Small-Angle Rotation in Individual Colloidal CdSe Quantum Rods

Zhiheng Yu,[†] Megan A. Hahn,[‡] Sara E. Maccagnano-Zacher,[§] Joaquin Calcines,[‡] Todd D. Krauss,[‡] Erik S. Alldredge,[†] and John Silcox[§,*]

[†]Physics Department, Cornell University, Ithaca, New York 14853, [‡]Chemistry Department, University of Rochester, Rochester, New York 14627, and [§]School of Applied and Engineering Physics, Cornell University, Ithaca, New York 14853

ABSTRACT CdSe quantum rods (QRs) are very promising novel materials with unique electronic and optical properties. In this paper, we utilize a broad spectrum of techniques including high-resolution annular dark field scanning transmission electron microscope imaging, electron nanodiffraction, and computer simulations to study the internal structure of individual QRs. Random small-angle rotations are commonly found between various sections within individual QRs which can be resolved into twists around the *c*-axis and bends. The possible origins of these small-angle rotations are further studied. We propose that imperfect oriented attachment coupled with electrostatic interactions between smaller nanoparticles during the growth process results in such small-angle rotations. These small-angle rotations may significantly affect the electronic and mechanical properties of CdSe QRs.

KEYWORDS: semiconductor nanorods · nanodiffraction · oriented attachment · electron microscopy

Colloidal CdSe quantum rods (QRs) are of great interest for fundamental research and are highly promising novel materials for new technology.[1,2] Most of the research interest regarding CdSe QRs has been focused on their unique electronic and optical properties since the optical and electronic properties of an individual QR depend strongly on its size and shape.[3] However, QR properties will also depend on the quality of their internal crystal structure since, for example, structural defects can serve as possible trapping sites for electrons or holes. Therefore, investigations of the internal crystalline structure of individual QRs are important.

The development of relatively simple chemical synthesis procedures has proven successful in generating QRs of nearly monodispersive distribution in shape and size.[4–7] The QR growth process is proposed to be a diffusion-controlled process in which atoms are preferentially added onto the two surfaces of high chemical activity[8] perpendicular to the *c*-axis.[6] This growth process[6,7] is a modification of the traditional crystal growth theory in which individual atoms or molecules are the basic building blocks that build up to make the crystal grow.[9] As a result of the dominant growth along the *c*-axis only, long QRs with aspect ratios of 1:10 can be produced.

A different nanoparticle growth mechanism, termed "oriented attachment", has also been proposed recently.[10–13] In this mechanism, nanoparticles consisting of hundreds or even thousands of atoms join together by sharing one common surface to minimize the total free energy. Some interesting nanostructures have been observed to support this mechanism, including oriented chains formed by aligned TiO_2 nanocrystals[13] and nanowires of PbSe formed from the oriented attachment of PbSe quantum dots.[14]

With the wurtzite structure, colloidal CdSe QRs possess net dipole moments along their *c*-axes.[15,16] When two nanoparticles come close to each other, interaction between the dipole moments may result (if strong enough) in an attractive force that could cause the two nanoparticles to merge. For example, upon controlled removal of the organic capping ligand on the nanoparticle surface, CdTe quantum dots spontaneously reorganized into crystalline nanowires and a strong dipole−dipole interaction was invoked as the driving force of this process.[17] The small dipole moment of PbSe quantum dots also was the driving force in the formation of nanowires through oriented attachment.[14] During the synthesis of CdSe QRs, the surface capping ligand (also the solvent) rapidly comes on and off the growing particles, allowing new monomers to bind to the surface. Thus, the idea of nanoparticles fusing together (driven by dipole−dipole interactions) during the

*Address correspondence to js97@cornell.edu.

Received for review October 25, 2007 and accepted May 21, 2008.

Published online June 24, 2008.
10.1021/nn700323v CCC: $40.75

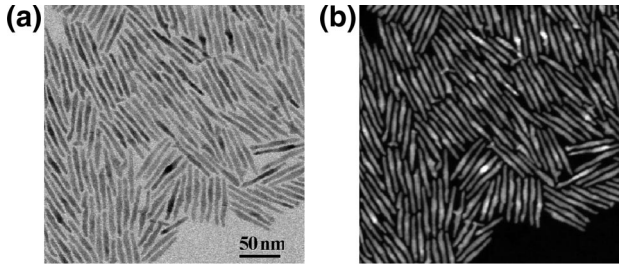

Figure 1. Low-magnification (200 000×) images of CdSe QRs recorded simultaneously on the Cornell VG HB501 100 kV UHV STEM. (a) BF image (comparable to normal TEM images), (b) ADF image. The shapes, sizes, and morphologies of the QRs are consistent with those of long QRs reported earlier.[4–7,24] Close inspection identifies contrast variations along individual QRs in the BF image.

synthesis to form a long QR through an oriented attachment process may still apply. In addition, the attachment process is likely to be imperfect, resulting in certain defects in the final product. Therefore, a detailed study of the internal structure of individual QRs is an important step in understanding critical details of the growth process.

High-resolution electron microscopy is an important research tool for the study of the structure of individual CdSe QRs. To a first approximation, a transmission electron microscope (TEM) image can be treated as a two-dimensional (2D) projection of a three-dimensional (3D) object. When the projection is not along a major zone axis, the resultant image usually exhibits 1D lattice fringes. However, under many circumstances, a TEM image with 1D lattice fringes may not give precise information about the structure of the object. In fact, sometimes misleading or even wrong information, such as false lattice spacings,[18] can be deduced from an image alone. For example, when a CdS QR was tilted away from the zone axis at particular angles, the projected 2D image appeared to show certain defects such as a twin or amorphous portions, purely due to atomistic overlapping at those tilt angles,[19] when in reality the QR had a perfect lattice.

Recently, the internal structure of individual CdSe QRs was investigated using scanning transmission electron microscopy (STEM). Electron nanodiffraction[20–22] from various sections along a single QR, coupled with computer simulations, provided detailed and unambiguous information about the internal structure of individual QRs.[23] Using nanodiffraction small-angle rotations between various sections of single QRs were detected and characterized for the first time. Electron nanodiffraction allowed for the collection of diffraction patterns from nanometer sized areas and thus provided detailed information about the lattice structure without possible ambiguities of interpreting a projected image. In addition, nanodiffraction provided precise information about the orientation of the crystal relative to the electron beam.

In this report, we explore the possible origins of the small-angle rotations seen along various sections of a single CdSe QR using electron nanodiffraction and conventional STEM imaging. We found strong evidence that oriented attachment plays a role during the growth process of long QRs with aspect ratios greater than 1:10, which would in turn cause these small-angle rotations. We provide estimates of possible forces that might be responsible for driving oriented attachment during growth of long QRs.

RESULTS AND DISCUSSIONS

Low-Magnification STEM Images—Contrast Variation. Figure 1 shows low-magnification bright field (BF) and annular dark field (ADF)[24] images of CdSe QRs obtained simultaneously that are comparable to TEM images reported in the literature.[4–7,25] The BF-STEM image is a phase-contrast image analogous to a conventional TEM BF image, so the signal from the QRs is relatively hard to distinguish from that of the carbon film. On the other hand, the ADF-STEM image reflects the atomic number Z-contrast between the carbon and the much heavier CdSe QR as well as thickness contrast. As a result, the QRs appear much brighter than the carbon film background.

Close inspection of the BF-STEM image of QRs in Figure 1 reveals contrast variation at different sections along the long axes of the QRs, whereby some sections of a QR may appear brighter (darker) than other sections of the same QR. This observation is also similar to low-magnification TEM images of CdSe QRs reported in the literature,[4–7,25,26] whereby intensity variations are seen along some individual QRs and along individual arms of CdTe tetrapods.[27] The phase-contrast nature of the BF images suggests that the incident fast electrons experience different scattering in various sections along a QR, which in turn suggests the structure and/or orientation of the QR may change along its long axis. However, the significance of the intensity variations along individual QRs has not been studied in detail.

Measurement of Small-Angle Rotation. To study the internal structure of individual QRs, high-resolution images containing lattice fringes and nanodiffraction patterns were taken from various sections along individual QRs. For example, Figure 2 shows a high-resolution ADF lattice image (small probe) from one end of a QR and a nanodiffraction pattern (large probe) from the center position. The indexed symmetric nanodiffraction pattern in Figure 2b suggests this portion of the QR is a wurtzite crystal aligned along the $(11\bar{2}0)$ zone axis. The projection along this zone axis with high symmetry results in the two-dimensional lattice fringes seen in Figure 2a. If the QRs were tilted off the zone axis, the projection would lose its high symmetry and one-dimensional lattice fringes would show up in the high-resolution image. From simply looking at images containing one-dimensional lattice fringes, it is difficult to

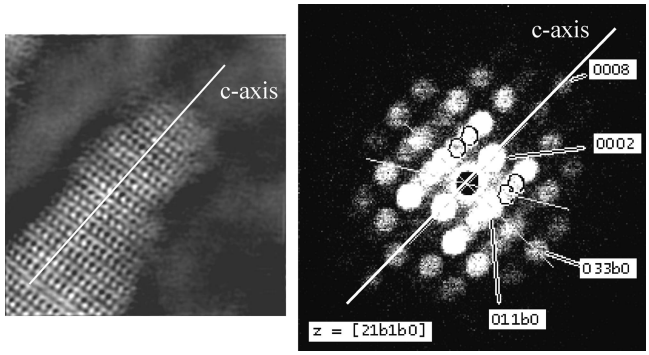

Figure 2. A high-resolution ADF image of a CdSe QR obtained by the small probe and the nanodiffraction pattern from the center obtained by the large probe. The nanodiffraction pattern suggests the QR is aligned on the (11$\bar{2}$0) zone axis.

tell the orientation of the QR or its lattice structure. In those situations, a nanodiffraction pattern is the only reliable method for getting at the internal structure.

Close inspection of the high-resolution lattice images suggests that the lattice pattern often changes along a single QR.[23] For example, the change of lattice pattern may be relatively transparent such as the observation of 1D and 2D lattice fringes alternating along the long axis of the QR.[23] On the other hand, sometimes the change in lattice pattern is not as obvious, as shown in Figure 3, where a low-magnification BF image of a QR is shown together with seven high-resolution BF lattice images from various sections of the QR. There are changes in the fringe pattern along the QR, although they are not necessarily obvious or striking. These changes can be understood more readily with the electron nanodiffraction patterns presented in Figure 4. The nanodiffraction patterns obtained from various positions on this QR are labeled as "A" to "I" and shown with a low-magnification ADF image giving the locations corresponding to the nanodiffraction patterns. All the nanodiffraction patterns from various places on the QR reveal a wurtzite structure consistent with powder X-ray diffraction results.[6,7] However, the nanodiffraction patterns indicate that the crystalline structure changes along the QR since the intensity distribution in the diffraction disks changes as one moves from A to I, indicating that the orientation of the QR relative to the incident beam changes along the QR long axis. Specifically, these patterns suggest that rotations exist between positions "A" to "D" and from "H" to "I", but that positions "E", "F", and "G" essentially have the same orientation.

To obtain information about the direction of the rotation axis and the magnitude of the rotation, multislice simulations[24] were carried out. A simulated CdSe QR with a diameter of 5 nm was constructed and oriented initially along the (11$\bar{2}$0) zone axis. This QR can be rotated about an arbitrary axis for an arbitrary angle, and the resultant nanodiffraction pattern at each posi-

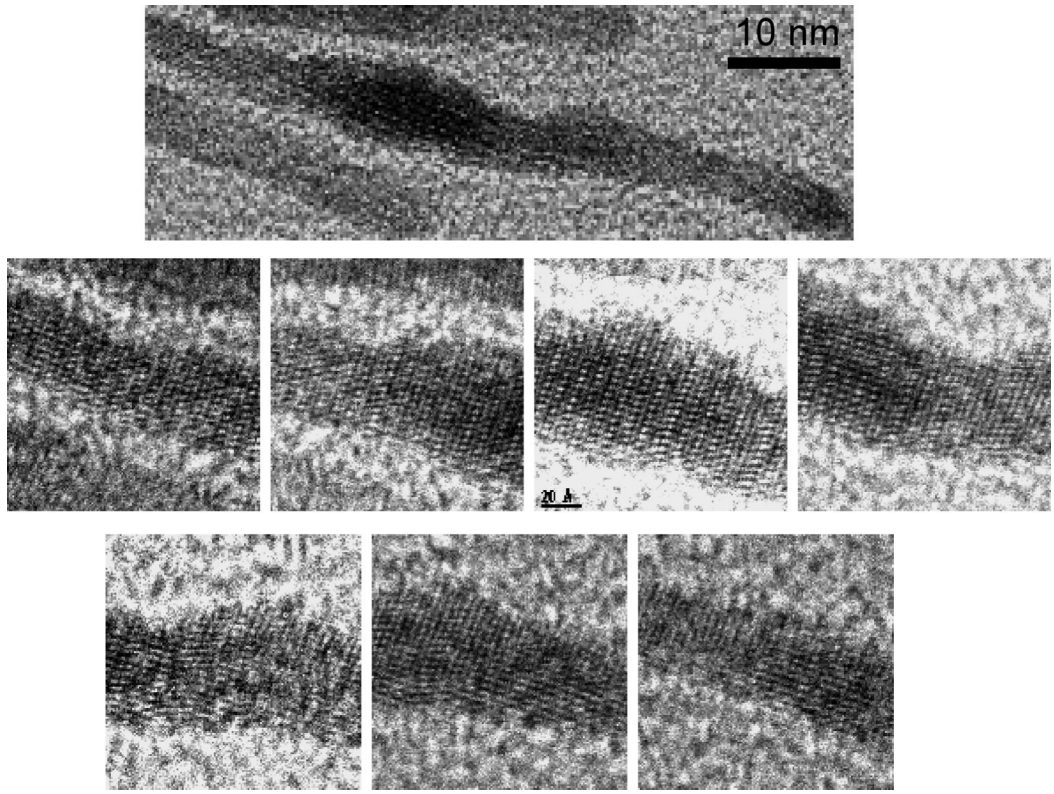

Figure 3. High-resolution BF images of a single QR. On the top is a low-magnification BF image of a single quantum rod. The bottom two rows show the high-resolution BF images from various places of the rod.

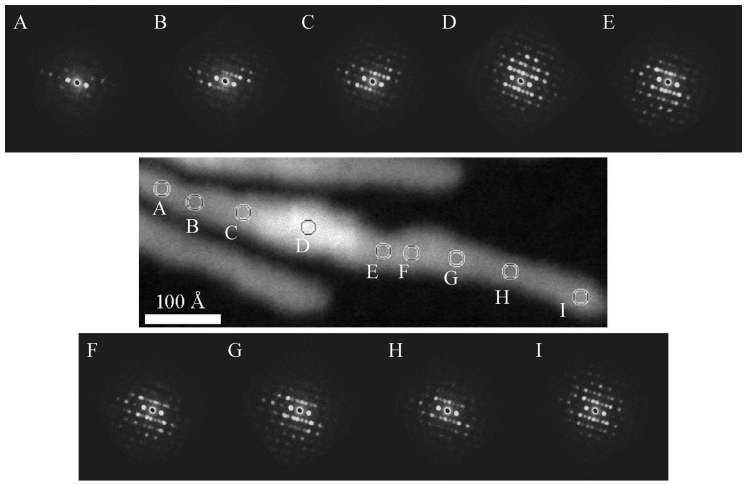

Figure 4. Low-magnification ADF image of the QR and electron beam nanodiffraction patterns from various positions labeled A to I on the QR. All the patterns suggest a wurtzite lattice. The intensity distribution in the nanodiffraction patterns changes from place to place, suggesting the orientation is different for different sections of the QR.

tion can be simulated. Figure 5 shows the simulated nanodiffraction patterns matching the experimental results in Figure 4. The indices on the upper right corners of the simulated patterns correspond to the labels in the experimental nanodiffraction patterns of Figure 4. The index (*x*,*y*) on the lower right corner of each pattern means the QR is tilted *y* degrees off the $(11\bar{2}0)$ zone axis about an axis *x* degrees off the *c*-axis of the QR. The step size/error bar is 2 degrees in *x* and is 0.2 degrees in *y*. Table 1 summarizes the topology of the QR shown in Figures 4 and 5. It is clear that small-angle rotations (typically 1−3 degrees) between different portions of a single QR exist, and the rotation axes may have substantial angles with the *c*-axis of the rod. Such a small-angle rotation can be defined as a combination of a small twist about the *c*-axis and a bend about an axis perpendicular to the *c*-axis as shown in Figure S1.

In all, we examined 20 QRs in detail, and in each case, the electron nanodiffraction patterns from all of these QRs indicate a wurtzite structure. In addition, small-angle rotations within these structures are commonly seen. Figure S2 shows low-magnification images of another QR and the nanodiffraction patterns taken from various places along the long axis. The small-angle lattice rotation within individual QRs is again observed with a random character. In other words, the rotation is not a smooth twist from one end of a QR to the other. The existence of small-angle rotations is independent of the shape of QRs since the QR in Figure S2 is straight without kinks or elbows. Nevertheless, some small-angle rotations still exist between various sections of the QRs as seen in the nanodiffraction patterns.

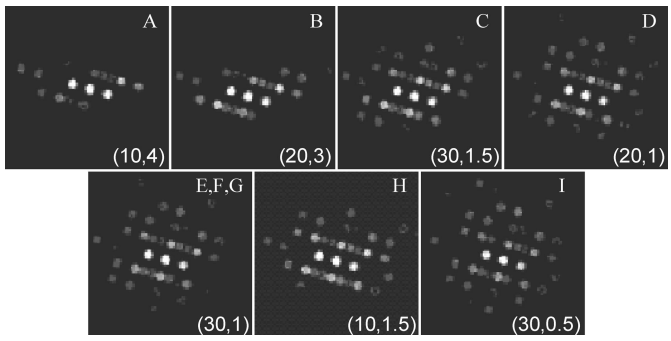

Figure 5. Simulated nanodiffraction patterns. The indices on the upper right corners refer to the labels of those matching experimental nanodiffraction patterns. The index (*x*,*y*) on the lower right corner of each pattern means the QR is rotated *y* degrees away from the $[11\bar{2}0]$ zone axis about an axis *x* degrees away from the *c*-axis of the QR. The error bar/step interval in *x* is 2° and 0.2° for *y*.

Generally, a change in the lattice patterns along a single QR may arise from two possible causes: (1) the orientation of different parts of the rod is not the same with respect to the incident electron beam, *i.e.*, some relative rotation exists between various portions of the rod; or (2) the crystal structure may change along the QR (say from wurtzite to zinc blende).[4] Electron nanodiffraction from various sections of individual QRs is a precise and direct method that provides local orientation details and indicates how these vary from point to point along the specimen. Electron micrographs of the interface regions between two areas of different orientation show that the interfaces are relatively sharp, spanning no more than two or three atomic layers and are similar to the small-angle grain boundaries seen in bulk material.

Origin of the Small-Angle Rotations: Exclusion of Screw Dislocation. The small-angle rotation between different portions of a single QR may be related to certain crystalline defects, such as a screw dislocation along the center of the QR. However, the experimental and simulated results in Figures 4, 5, and 6 suggest the exclusion of a screw dislocation as the origin of twisting. A screw dislocation inside a finite rod or a thin long whisker produces the well-known Eshelby twist along the object.[28–31] The resultant twist is uniform and continuous, and its amplitude per unit length is given by the equation[32]

$$\varphi = \frac{-b}{\pi R^2} \qquad (1)$$

where *b* is the amplitude of the Burgers vector describing the screw dislocation and *R* is the radius of the rod. For $b = 0.35$ nm (the atomic spacing along the *c*-axis) and $R = 2.5$ nm, eq 1 predicts a uniform continuous twist per unit length of 1°/nm. This twist magnitude is too large by an order of magnitude in comparison with the value determined for the QR shown in Figure 3. For example, points A and D (Figure 4) are separated by about 30 nm, resulting in a relative Eshelby twist of roughly 30° between these two portions. However, the detected twist is only about 3°. Also, the detected twist in the QR is not continuous, as expected for an

TABLE 1. Topology of the Single QR in Figures 4 and 5: Angle *y* Is the Rotation Angle Away from the [11$\bar{2}$0] Zone Axis, and *x* Is the Angle between the Rotation Axis and the *c*-Axis

position	A	B	C	D	E	F	G	H	I
rotation angle *y*	4°	3°	1.5°	1°	1°	1°	1°	1.5°	0.5°
rotation axis *x*	10°	20°	30°	20°	30°	30°	30°	10°	30°

Eshelby twist. For example, from points E to G in Figure 4, there is essentially no twist and from H to I the twist direction is opposite to that from A to B.

Origin of the Small-Angle Rotations: Spontaneous Polarization and Dipolar Interaction. We suggest that the small-angle rotation within individual QRs may be associated with certain details of the growth process. During the growth, electrostatic forces will exist between neighboring QRs. These forces arise from the surface charges carried by the QRs due to their spontaneous internal polarization and likely play a significant role in the growth of long QRs. In this section, we estimate the possible net electrical charges carried by a QR and the magnitude of the associated electrostatic forces.

The noncentrosymmetric structure of a wurtzite crystal gives rise to a permanent polarization in any wurtzite material. This polarization is a complicated quantum phenomenon, and a simple treatment based solely on summing the dipole moments of a unit cell is incorrect.[33–35] In order to get a good theoretical estimate of the magnitude of the internal polarization in CdSe QRs, detailed calculations were carried out using the Berry phase method[36,37] applied with first-principles calculations based upon density functional theory. Specifically, we employed the Vienna *ab initio* Simulations Package (VASP),[38–40] which uses a plane wave basis for wave functions combined with ultrasoft pseudopotentials[41] (Cd d electrons are treated as valence electrons). Calculations were made with both the local density approximation (LDA), using the correlation energy of Ceperley and Alder,[42,43] and the generalized gradient approximation (GGA) in the Perdew−Wang

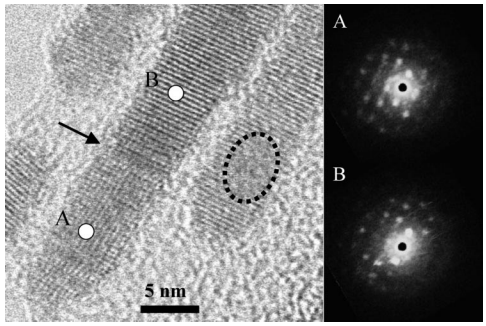

Figure 6. A high-resolution BF image showing evidence of oriented attachment and the nanodiffraction patterns from two positions on it: The arrow indicates a clear boundary between shorter QRs. The nanodiffraction patterns suggest the two portions are rotated slightly. The ellipse indicates a smaller particle that was absorbed onto the QR that subsequently grew around it.

TABLE 2. Structural Parameters and Polarization of Wurtzite CdSe Calculated by LDA and GGA Methods and Compared with Experimental Values

	a (Å)	*c*/*a*	*P* (μC/cm^2)
LDA	4.257	1.632	0.5 ± 0.2
GGA	4.385	1.633	0.6 ± 0.2
experiment	4.2999	1.6305	0.19

PW91 version.[44,45] All calculations for wurtzite CdSe were performed using a Monkhorst-Pack mesh[46] of (12,12,12) for the *k*-space integration, while a value of 300 eV was set for the plane wave energy cutoff. Structural parameters were optimized, starting from experimental values, by determining Hellmann−Feynman forces and updating the positions of ions until the total energy was minimized. With the relaxed structures, we then used the Berry phase technique to calculate the spontaneous polarization of wurtzite CdSe. The results for both LDA and GGA are summarized in Table 2 together with experimental values for the lattice constants.[47]

The calculated spontaneous polarization is 0.5 ± 0.2 μC/cm^2 from the LDA method and 0.6 ± 0.2 μC/cm^2 from the GGA method. The spontaneous polarization along the *c*-axis results in net bound surface charges on the {0001} surfaces. Given that surface charges arising at the ends of the QRs would be screened by the dielectric response of the CdSe, it also seems appropriate to use the somewhat lower experimental value, 0.19 μC/cm^2 measured by a transient electric birefringence method[15] to estimate these charges. For a typical QR approximated as a cylinder with a diameter of 5 nm, a spontaneous polarization of 0.2 μC/cm^2 gives a net charge on the {0001} surfaces of $q = P \times \pi R^2 = 0.24$ e, *i.e.*, 24% of an elementary charge. In other words, the two surfaces perpendicular to the *c*-axis carry a charge of +0.24 and −0.24 e, respectively. In contrast, if the theoretical value of 0.6 μC/cm^2 is assumed, then the charges on the rod surfaces are ±0.6 e.

To get a sense of the magnitude of the electrostatic force between neighboring QRs, we report a crude estimate for a simple case when two long QRs are aligned along their *c*-axes. The positive end of one QR is facing the negative end of the other QR. We also model the QR growth solution as pure tri-*n*-octylphosphine oxide (TOPO) with a dielectric constant of $\epsilon = 2.5$.[48] Since the Coulomb interaction is inversely proportional to the square of distance and the dielectric constant of CdSe is 9, the dominant component of the electrostatic interaction between the two QRs is the attractive force between the two facing (oppositely charged) surfaces. When the two oppositely charged surfaces are very close to each other, the force between them can be modeled as a capacitive like force: $F = 1/2 \times Q^2/\varepsilon\varepsilon_0 A$, where Q and $A = \pi R^2$ are, respectively, the charge and area of one surface. Using $Q = 0.6$ e and $R = 2.5$ nm, we

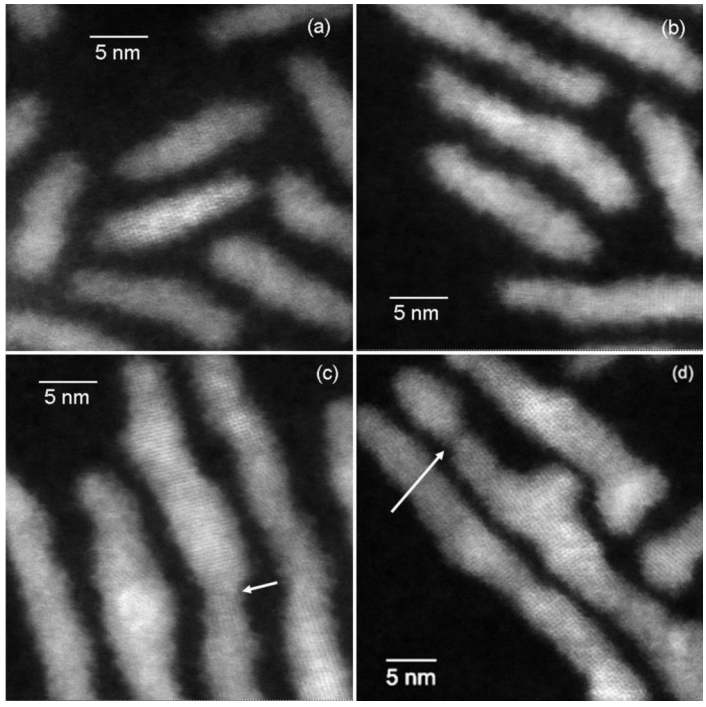

Figure 7. High-resolution ADF images of QRs of four different samples. Images a−c represent samples gathered and washed for STEM images after (a) 10 min, (b) 20 min, and (c) 1 h of growth. The sample in (d) is the supernatant of the washed sample after 45 min of growth. The white arrows in (c) and (d) show narrow necks in the larger QRs that suggest a join between two nanoparticles. The nanoparticles on either side of the neck also show differing lattice fringes, suggesting the crystal orientation between the two joining particles is slightly different.

calculated the attractive force between the two QRs as $F = 1.06 \times 10^{-11}$ N. Assuming the distance between the two oppositely charged surfaces is $d = 5$ nm, the potential energy due to the attractive force $E_P = Fd = 5.3 \times 10^{-20}$ J. If we use 0.24 e for the rod charges, corresponding to the experimental value, then the corresponding value for F is reduced to 1.7×10^{-12} N and that for E_p becomes 8.5×10^{-21} J. These values are at least comparable with, but somewhat larger than, the thermal energy at 300 °C (roughly the growth temperature) which is $k_BT = 7.9 \times 10^{-21}$ J with $k_B = 1.38 \times 10^{-23}$ J/K as the Boltzmann constant. This suggests competing driving forces (oriented attachment and diffusion controlled) in the crystal growth process compatible with formation of QRs with the type of structure exhibited in our observations.

The electrostatic interaction should facilitate the attraction between two QRs, which will further be driven to attach by a reduction of their surface energy resulting in a longer QR. The above calculation is for a very special case when two QRs are aligned along their *c*-axes. In general, the relative position of two QRs is arbitrary, and the electrostatic interaction between them may result in different configurations. The existence of multiple neighboring QRs in the solution makes the situation much more complicated. Nevertheless, for even a completely random mixture of dipolar molecules in a fluid, the formation of chains is certainly possible. For example, various theoretical works suggest the formation of chains in a fluid consisting of dipole molecules due to the dipolar interaction,[49–51] with recent progress reported by Huang and Lai.[52] In fact, the recent observation that quantum dots of CdTe[17] and PbSe[14] reorganized into highly crystalline nanowires provides direct experimental support that this idea is reasonable.

Origin of the Small-Angle Rotations: Oriented Attachment. Independent of any electrostatic interaction during solution growth, smaller nanocrystals may fuse to form bigger nanoparticles, which is the essence of a crystal growth model proposed by Penn and Banfield.[10–13] This "oriented attachment" model states that under some growth conditions the basic synthetic building blocks are nanoparticles and not individual atoms or molecules. Attachment is energetically favored because it rids the system of extra surfaces and their associated higher surface energies. For example, aligned chains of TiO_2 nanocrystals grew according to an oriented attachment process despite the lack of an electrostatic interaction between the nanocrystals.

The shift in long-range coordination represented by the observed changes in crystal orientation along the nanorods implies the nanorod may be composed of several smaller nanoparticles with a collective lattice shift of one nanoparticle relative to another. This idea can be intuitively explained *via* oriented attachment. We therefore suggest that in addition to diffusion-controlled crystal growth a parallel process can occur in which two shorter QRs can attach to form longer QRs in an oriented attachment fashion driven by the electrostatic forces briefly outlined above. This attachment is favored along the *c*-axis due to the following: first, the {0001} surfaces perpendicular to the *c*-axis have a higher chemical reactivity and, second, a higher chemical potential on these surfaces. Earlier, this was discussed as the main driving force for the growth along the *c*-axis in a completely diffusion growth model.[6,7] We are suggesting here that, as the particles grow in size and surface charges begin to develop on selected surfaces, the electrostatic terms play a larger role in the growth process.

Strong evidence for the idea that oriented attachment may play a role in the formation of larger QRs comes from high-resolution STEM images. As shown in Figure 6, from the high-resolution BF lattice image of a single QR, one can tell easily that the bottom portion (position A) is clearly different from the central portion (position B). The arrow indicates a sharp interface between these two regions. It is straightforward to regard the bottom portion and the central portion as two separate smaller QRs attached to each other. The two regions are not in complete alignment, and the relative rotation between them is small (~2°), as suggested by the nanodiffraction patterns. A second example is the rightmost QR in the same image. The dashed ellipse encloses a region where no lat-

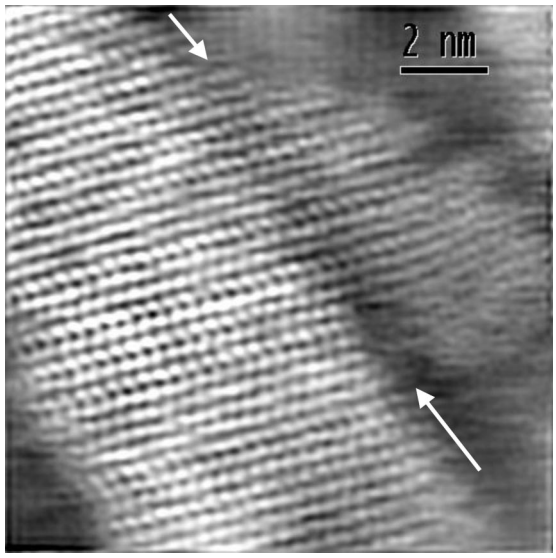

Figure 8. A high-resolution ADF lattice image (at 5 000 000×) of a QR. A small particle is attached to a QR from the side. Lattice fringes run across the interface between them. The arrow indicates a thinner connection region (darker means thinner for ADF images) between these two parts.

tice fringes are seen. The fact that lattice fringes are seen in all the areas surrounding the ellipse suggests that a smaller nanoparticle (enclosed by the ellipse) was absorbed on the QR. To determine at what point during the growth the QRs exhibit the features of oriented attachment as discussed in this study, specimens were extracted from a sample of CdSe QRs at different times along the growth process. Figure 7 shows high-resolution ADF images of these QRs after 10 min (Figure 7a) and 20 min (Figure 7b) of growth, respectively. These shorter QRs with average lengths of 13.9 and 22.2 nm, respectively, show none of the shifts of lattice fringes as seen in the longer rods. Figure 7c,d shows QRs after 1 h and 45 min of growth, respectively, with average lengths of 44.9 and 39.8 nm, respectively, and the crystal lattice shifts along the length of these QRs are clearly evident. Thus, as the nanorods grow beyond 25 nm, oriented attachment is starting to dominate the growth of larger species.

ADF imaging provides thickness contrast with thicker specimen areas appearing brighter in ADF images, which can also be used to illustrate evidence of oriented attachment contributing to nanorod growth. The white arrows in Figures 7c,d point to thinner sections between two brighter, thicker sections. These thicker sections can be treated as individual nanoparticles comprising a QR. To be specific, the arrow in Figure 7d points to a thinner neck connecting two thicker nanoparticles. This observation is consistent with the picture that, as two cylindrical objects attach, the connection region between them is thinner than the centers of both objects. Upon closer observation of Figure 7d, the two thicker nanoparticles on either side of the white arrow appear to have different crystal orientations, suggested by the different lattice fringes in the nanoparticles. A similar observation can be made between the two nanoparticles on either side of the white arrow in Figure 7c.

In the original observations of oriented attachment,[12,13] longer nanoparticle chains were observed and the individual nanoparticle subunits comprising a chain were easily identifiable. Similar chains of particles were observed in the very early stages of long QR formation from individual CdTe spherical nanocrystals.[17] On the other hand, in our images, we have not observed linear chains of nanoparticles. However, we feel this is consistent with the proposal of oriented attachment also occurring for numerous reasons. First, the very high aspect ratio QRs we studied were removed from the growth solution after 1 h of growth time, providing ample time for smaller QRs to completely fuse. Second, QR growth forms only under a high monomer concentration. Since both oriented attachment and diffusion-controlled growth likely coexist and complement each other during the growth process in solution, we can expect that highly reactive monomers can fill in the "gaps" between two oriented QRs efficiently and relatively quickly. One such example is the formation of an elbow between a QR and an attached nanoparticle.[23] Finally, even without the presence of monomers, uniform cylindrical rods of CdTe nanoparticles were formed by simply allowing spherical nanoparticles to coalesce.[17] Thus, we could expect similar behavior from the attachment between two QRs.

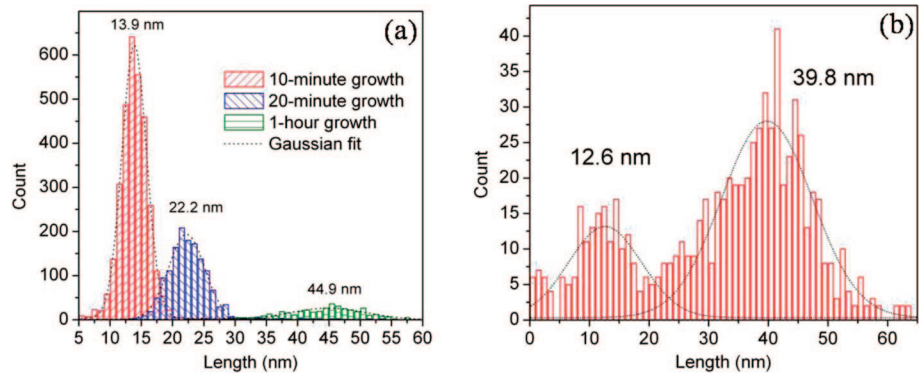

Figure 9. Histograms of the lengths of the rods in four samples of CdSe QRs whose images are shown in Figure 7. The histograms in (a) show the single-peak character and average lengths found in the 10 min (~14 nm), 20 min (~22 nm), and 1 h (~45 nm) growth samples. The histogram in (b) represents a 45 min growth sample pulled out of the supernatant during STEM sample preparation. The histogram shows two distinct peaks, suggesting the existence of two standard lengths of rods in the sample. The larger peak represents rods with an average length of ~40 nm, which is the expected length for this sample's preparation time. The smaller peak represents rods with an average length of ~13 nm.

We have also observed other attachment configurations besides end-to-end attachment. The ADF image in Figure 8 shows a rare case of sidewall attachment, the only one seen in ~200 images. A small QR is seen to attach to a larger one from the side, with arrows indicating the attachment interface. The interface appears darker, and therefore, the connection region between the two QRs is thinner. The ADF image is good evidence that the smaller QR did not "grow" out of the larger one and instead it is attached from one side. The fact that lattice fringes run all the way from the big QR to the small QR through the thinner connection region suggests that the attachment occurs on atomic scale.

If oriented attachment is the source of the observed changes in crystal orientation and also thus contributes to the nanorod growth process, then we can expect that the nanorod growth solution should contain smaller as well as larger rods. Typical sample processing for STEM imaging involves careful removal of the TOPO, which involves precipitating the nanorods with a nonsolvent followed by centrifugation and dilution to a density suitable for electron microscopy. This process is also used to separate larger nanoparticles from smaller ones and thus causes larger particles to be kept while smaller ones in the supernatant are typically discarded. Indeed, the length histograms of the three nanorod samples prepared for STEM imaging in the standard way, with typical images as shown in Figures 7a−c, have only one peak that is fitted well with a Gaussian distribution (Figure 9a).

To determine the nature of the particles that are normally discarded during the "washing" process, we collected and examined some of the previously discarded supernatant product. In Figure 9b, we show a length histogram of nanorods from a supernatant sample taken from a 45 min growth solution after a single wash. An image of the QRs in this sample is shown in Figure 7d. The histogram of the nanorod length in the supernatant shows two distinct peaks, giving evidence to the presence of smaller particles, which were also seen in low-magnification images (not shown). The bimodal length distribution is in stark contrast to the length histograms of the three samples prepared for STEM imaging in the standard way, which displayed only a single Gaussian distribution.

Consequences of Imperfection. We propose that the physical properties of the QRs will be altered, perhaps considerably, because of their imperfections, as has already been detected in electrostatic force microscopy studies of the surface charges carried by the QRs.[53] Mechanical properties will also be changed. For example, a QR with no imperfections or defects can be very robust under stress. However, in the presence of imperfections resulting from oriented attachment, the mechanical properties should be weaker than expected for a perfect crystal since fracture of the QRs would occur preferentially at the joints between the nanoparticles. These changes in the physical properties will certainly impact the development of potential technical applications based on QRs.

CONCLUSIONS

The small electron probe available through STEM provides a perfect tool to study the internal structure of individual CdSe QRs. We operated the STEM under two different optical conditions to generate a small probe (0.2 nm) and a large probe (~1 nm). The small probe was used to get high-resolution images with lattice fringes, and the large probe was fixed on various positions of a single QR to get nanodiffraction patterns. The combination of these techniques allowed us to measure local crystalline structure and orientation information from an area of 1 nm × 1 nm.

Electron nanodiffraction patterns from various locations on individual QRs confirm wurtzite as the crystal structure of the QRs. The intensity distribution in the nanodiffraction pattern changes as the probe is located at different locations on a single QR. This suggests that it is common to find rotations between various sections of individual QRs. The rotations were calibrated by matching multislice simulated nanodiffraction patterns with the experimental ones. It is found that the rotations are small angle (only a couple of degrees) but the rotation axes form substantial angles with the *c*-axis of the QR.

We propose that imperfect oriented attachment is the origin of the small-angle rotations. During the growth, two neighboring shorter QRs may attach to each other to form a longer QR. The existence of surface charges on the {0001} faces due to the spontaneous internal QR polarization is likely to facilitate the attachment. These imperfections may significantly affect the optical and electronic property of the QRs. Mechanical properties are also weakened, and the QRs can be fractured easily at the joints between different nanoparticles.

METHODS

CdSe quantum rods with diameters of 5−6 nm and aspect ratios from 1:10 to 1:16 were synthesized according to variations of literature procedures.[6,7,25] Specimens for electron microscopy were obtained by the addition of methanol and butanol to the suspension to allow the QRs to fall out of suspension and centrifugation at ~2000*g* for several minutes. This results in a pellet of particles below a liquid supernatant. The pellet of particles was separated from the supernatant and resuspended in hexane. This washing process may be repeated several times. The electron microscopy specimens were made by depositing a ~10 μL drop of the hexane solution onto a holey carbon film covered copper grid. Scanning transmission electron microscopy on a Cornell VG HB501 100 kV UHV STEM was used to study single CdSe QR internal structure. A nanometer-sized STEM probe was fixed on certain sections of a QR to get electron beam nanodiffraction patterns.

A 0.2 nm STEM probe was used to obtain high-resolution BF and ADF images with lattice fringes resolved. This value arises from a balance between the phase shifts due to defocus on one hand and those due to spherical aberration on the other hand.[54] The associated beam current is also at a minimum at the electron optical settings needed to achieve such a small probe size. The STEM probe is formed by the objective lens before reaching the specimen. An objective aperture is used to set the convergent angle of the probe and the beam current enclosed in the probe. Spherical aberration of the objective lens determines the size of the objective aperture that produces the optimized probe size d_0 (which in turn determines the resolution) with a convergent angle α_0. For the same objective lens, a smaller convergent angle ($<\alpha_0$) corresponds to a larger probe size ($>d_0$). Figure S3 shows three simulated probe profiles at different convergent angles with all other optical parameters fixed. Electron optical conditions with an acceleration voltage of 100 kV and a spherical aberration of C_s = 1.3 mm are representative of the Cornell STEM.

The probe generated by the 10 mrad objective aperture (the physical size of this objective aperture is ~40 μm) is ~2 Å fwhm in size. It is used to obtain high-resolution BF and ADF images with lattice fringes resolved. However, this probe is not ideal for the collection of electron diffraction patterns because it has a large convergence angle of 10 mrad that broadens the diffraction spots into diffraction disks with a radius of 10 mrad, causing the diffraction disks to overlap. On the other hand, a diffraction pattern generated by a larger probe with a smaller convergence angle (say, 2.5 mrad) is much simpler and easier to interpret. Therefore, we collect a diffraction pattern with a probe of nanometer size and a small convergence angle (2−4 mrads) (referred to as nanodiffraction patterns).[20−22]

We found that the nanodiffraction patterns from individual CdSe QRs collected with the probe formed by a ~10 μm aperture (corresponding to ~2.5 mrad) are very noisy. Weak high-order diffraction disks that are useful in determining the lattice structure and orientation are lost due to the poor signal/noise ratio. Therefore, it is critical to increase the beam current while keeping the convergence angle small. By using a different condenser setting to defocus the electron beam, we found an operating condition that achieved a 2−4 mrad convergence angle at a probe size of 0.7−1.5 nm. This enabled us to obtain localized nanodiffraction patterns from various points along a single QR. Previous work enabled us to work with a beam current that did not damage the sample.

Statistics of the length of the QRs were collected using commercial image analysis software (Digital Micrograph). The edges of the particles were found by choosing from the image intensity histogram all of the intensities due to the QRs in the image and thereby separating the QRs from the carbon substrate. These particles were then analyzed by the software, producing values for average length and width for each particle in the image.

Acknowledgment. This work was supported by the Nanoscale Science and Engineering Initiative of the National Science Foundation under NSF Award Number EEC-0117770. Funding for the growth of quantum rods was supported by the NSF (CHE 0616378) and the Air Force Office of Scientific Research (FA9550-04-1-0430). We thank M. Thomas for assistance in getting nanodiffraction data, and E.J. Kirkland for providing image filters.

Supporting Information Available: Figures showing an illustration of the lattice twist, additional STEM images of the nanorods, and STEM probe profiles. This material is available free of charge *via* the Internet at http://pubs.acs.org.

REFERENCES AND NOTES

1. Huynh, W. U.; Dittmer, J. J.; Alivisatos, A. P. Hybrid Nanorod-Polymer Solar Cells. *Science* **2002**, *295*, 2425–2427.
2. Kazes, M.; Lewis, D. Y.; Ebenstein, Y.; Mokari, T.; Banin, U. Lasing from Semiconductor Quantum Rods in a Cylindrical Microcavity. *Adv. Mater.* **2002**, *14*, 317–321.
3. Alivisatos, A. P. Semiconductor Clusters, Nanocrystals, and Quantum Dots. *Science* **1996**, *271*, 933–937.
4. Manna, L.; Scher, E. C.; Alivisatos, A. P. Synthesis of Soluble and Processable Rod-, Arrow-, Teardrop-, and Tetrapod-Shaped CdSe Nanocrystals. *J. Am. Chem. Soc.* **2000**, *122*, 12700–12706.
5. Peng, X. G.; Manna, L.; Yang, W. D.; Wickham, J.; Scher, E.; Kadavanich, A.; Alivisatos, A. P. Shape Control of CdSe Nanocrystals. *Nature* **2000**, *404*, 59–61.
6. Peng, Z. A.; Peng, X. G. Mechanisms of the Shape Evolution of CdSe Nanocrystals. *J. Am. Chem. Soc.* **2001**, *123*, 1389–1395.
7. Peng, Z. A.; Peng, X. G. Nearly Monodisperse and Shape-Controlled CdSe Nanocrystals *via* Alternative Routes: Nucleation and Growth. *J. Am. Chem. Soc.* **2002**, *124*, 3343–3353.
8. Puzder, A.; Williamson, A. J.; Zaitseva, N.; Galli, G.; Manna, L.; Alivisatos, A. P. The Effect of Organic Ligand Binding on the Growth of CdSe Nanoparticles Probed by *Ab Initio* Calculations. *Nano Lett.* **2004**, *4*, 2361–2365.
9. Mullin, J. W. In *Crystallization*; Butterworth: London, 1961; pp 101–135.
10. Alivisatos, A. P. Biomineralization: Naturally Aligned Nanocrystals. *Science* **2000**, *289*, 736–737.
11. Banfield, J. F.; Welch, S. A.; Zhang, H. Z.; Ebert, T. T.; Penn, R. L. Aggregation-Based Crystal Growth and Microstructure Development in Natural Iron Oxyhydroxide Biomineralization Products. *Science* **2000**, *289*, 751–754.
12. Penn, R. L.; Banfield, J. F. Oriented Attachment and Growth, Twinning, Polytypism, and Formation of Metastable Phases: Insights from Nanocrystalline TiO_2. *Am. Mineral.* **1998**, *83*, 1077–1082.
13. Penn, R. L.; Banfield, J. F. Morphology Development and Crystal Growth in Nanocrystalline Aggregates under Hydrothermal Conditions: Insights from Titania. *Geochim. Cosmochim. Acta* **1999**, *63*, 1549–1557.
14. Cho, K. S.; Talapin, D. V.; Gaschler, W.; Murray, C. B. Designing PbSe Nanowires and Nanorings through Oriented Attachment of Nanoparticles. *J. Am. Chem. Soc.* **2005**, *127*, 7140–7147.
15. Li, L. S.; Alivisatos, A. P. Origin and Scaling of the Permanent Dipole Moment in CdSe Nanorods. *Phys. Rev. Lett.* **2003**, *90*, 097402/1–097402/4.
16. Shim, M.; Guyot-Sionnest, P. Permanent Dipole Moment and Charges in Colloidal Semiconductor Quantum Dots. *J. Chem. Phys.* **1999**, *111*, 6955–6964.
17. Tang, Z. Y.; Kotov, N. A.; Giersig, M. Spontaneous Organization of Single CdTe Nanoparticles into Luminescent Nanowires. *Science* **2002**, *297*, 237–240.
18. Malm, J. O.; OKeefe, M. A. Deceptive "Lattice Spacings" in High-Resolution Micrographs of Metal Nanoparticles. *Ultramicroscopy* **1997**, *68*, 13–23.
19. Ascencio, J. A.; Santiago, P.; Rendon, L.; Pal, U. Structural Basis for Homogeneous CdS Nanorods: Synthesis and HREM Characterization. *Appl. Phys. A: Mater. Sci. Process.* **2004**, *78*, 5–7.
20. Cowley, J. M. Electron Nanodiffraction. *Microsc. Res. Technol.* **1999**, *46*, 75–97.
21. Cowley, J. M. Applications of Electron Nanodiffraction. *Micron* **2004**, *35*, 345–360.
22. Cowley, J. M. Electron Nanodiffraction: Progress and Prospects. *J. Electron Microsc.* **1996**, *45*, 3–10.
23. Yu, Z. H.; Hahn, M. A.; Calcines, J.; Krauss, T. D.; Silcox, J. Study of the Internal Structure of Individual CdSe Quantum Rods using Electron Nanodiffraction. *Appl. Phys. Lett.* **2005**, *86*, 013101-1–013101-3.
24. Kirkland, E. J. In *Advanced Computing in Electron Microscopy*; Plenum Press: New York, 1998; pp 99–150.
25. Peng, Z. A.; Peng, X. G. Formation of High-Quality CdTe, CdSe, and CdS Nanocrystals Using CdO as Precursor. *J. Am. Chem. Soc.* **2001**, *123*, 183–184.
26. Hu, J. T.; Li, L. S.; Yang, W. D.; Manna, L.; Wang, L. W.; Alivisatos, A. P. Linearly Polarized Emission from Colloidal Semiconductor Quantum Rods. *Science* **2001**, *292*, 2060–2063.

27. Manna, L.; Milliron, D. J.; Meisel, A.; Scher, E. C.; Alivisatos, A. P. Controlled Growth of Tetrapod-Branched Inorganic Nanocrystals. *Nat. Mater.* **2003**, *2*, 382–385.
28. Dragsdorf, R. D.; Webb, W. W. Detection of Screw Dislocations in α-Al_2O_3 Whiskers. *J. Appl. Phys.* **1958**, *29*, 817–819.
29. Drum, C. M. Axial Imperfections in Filamentary Crystals of Aluminum Nitride. *J. Appl. Phys.* **1965**, *36*, 816–823.
30. Eshelby, J. D. Screw Dislocations in Thin Rods. *J. Appl. Phys.* **1953**, *24*, 176–179.
31. Webb, W. W. Point Defect Trapping in Crystal Growth. *J. Appl. Phys.* **1962**, *33*, 1961–1971.
32. Hirth, J. P.; Lothe, J. *Theory of Dislocations* McGraw-Hill: New York, 1968; p 61.
33. Kingsmith, R. D.; Vanderbilt, D. Theory of Polarization of Crystalline Solids. *Phys. Rev. B* **1993**, *47*, 1651–1654.
34. Resta, R. Macroscopic Polarization in Crystalline Dielectrics—The Geometric Phase Approach. *Rev. Mod. Phys.* **1994**, *66*, 899–915.
35. Vanderbilt, D.; Kingsmith, R. D. Electric Polarization as a Bulk Quantity and its Relation to Surface-Charge. *Phys. Rev. B* **1993**, *48*, 4442–4455.
36. Bernardini, F.; Fiorentini, V.; Vanderbilt, D. Spontaneous Polarization and Piezoelectric Constants of III−V Nitrides. *Phys. Rev. B* **1997**, *56*, 10024–10027.
37. Resta, R. Theory of the Electric Polarization in Crystals. *Ferroelectrics* **1992**, *136*, 51–55.
38. Kresse, G.; Furthmuller, J. Efficiency of *Ab Initio* Total Energy Calculations for Metals and Semiconductors using a Plane-Wave Basis Set. *Comput. Mater. Sci.* **1996**, *6*, 15–50.
39. Kresse, G.; Furthmuller, J. Efficient Iterative Schemes for *Ab Initio* Total-Energy Calculations using a Plane-Wave Basis Set. *Phys. Rev. B* **1996**, *54*, 11169–11186.
40. Kresse, G.; Hafner, J. *Ab Initio* Molecular-Dynamics for Liquid-Metals. *Phys. Rev. B* **1993**, *47*, 558–561.
41. Vanderbilt, D. Soft Self-Consistent Pseudopotentials in a Generalized Eigenvalue Formalism. *Phys. Rev. B* **1990**, *41*, 7892–7895.
42. Ceperley, D. M.; Alder, B. J. Ground State of the Electron Gas by a Stochastic Method. *Phys. Rev. Lett.* **1980**, *45*, 566–569.
43. Perdew, J. P.; Zunger, A. Self-Interaction Correction to Density-Functional Approximations for Many-Electron Systems. *Phys. Rev. B* **1981**, *23*, 5048–5079.
44. Perdew, J. P.; Chevary, J. A.; Vosko, S. H.; Jackson, K. A.; Pederson, M. R.; Singh, D. J.; Fiolhais, C. Atoms, Molecules, Solids, and Surfaces-Applications of the Generalized Gradient Approximation for Exchange and Correlation. *Phys. Rev. B* **1992**, *46*, 6671–6687.
45. Perdew, J. P.; Chevary, J. A.; Vosko, S. H.; Jackson, K. A.; Pederson, M. R.; Singh, D. J.; Fiolhais, C. Erratum: Atoms, Molecules, Solids, and Surfaces—Applications of the Generalized Gradient Approximation for Exchange and Correlation. *Phys. Rev. B* **1993**, *48*, 4978.
46. Monkhorst, H. J.; Pack, J. D. Special Points for Brillouin-Zone Integrations. *Phys. Rev. B* **1976**, *13*, 5188–5192.
47. Singh, J. *Physics of Semiconductors and Their Heterostructures*; McGraw-Hill, New York, 1993; Frontispiece.
48. Jiang, J.; Krauss, T. D.; Brus, L. E. Electrostatic Force Microscopy Characterization of Trioctylphosphine Oxide Self-Assembled Monolayers on Graphite. *J. Phys. Chem. B* **2000**, *104*, 11936–11941.
49. Degennes, P. G.; Pincus, P. A. Correlations in a Ferromagnetic Colloid. *Phys. Kondens. Mater.* **1970**, *11*, 189–198.
50. Jordan, P. C. Association Phenomena in a Ferromagnetic Colloid. *Mol. Phys.* **1973**, *25*, 961–973.
51. Jordan, P. C. Field-Dependent Chain Formation by Ferromagnetic Colloids. *Mol. Phys.* **1979**, *38*, 769–780.
52. Huang, J. Y.; Lai, P. Y. Formation and Polarization of Dipolar Chains. *Phys. A* **2000**, *281*, 105–111.
53. Krishnan, R.; Hahn, M. A.; Yu, Z.; Silcox, J.; Fauchet, P. M.; Krauss, T. D. Polarization Surface-Charge Density of Single Semiconductor Quantum Rods. *Phys. Rev. Lett.* **2004**, *92*, 216803-1–216803-4.
54. Scherzer, O. The Theoretical Resolution Limit of the Electron Microscope. *J. Appl. Phys.* **1949**, *20*, 20–29.